nature communications

Article

https://doi.org/10.1038/s41467-025-59625-1

A molecularly engineered large-area nanoporous atomically thin graphene membrane for ion separation

Received: 11 September 2024

Accepted: 24 April 2025

Ziwen Dai[1], **Pengrui Jin**[2], **Shushan Yuan**[1], **Jiakuan Yang**[1], **Kumar Varoon Agrawal**[3] & **Huanting Wang**[4]

Atomically thin graphene membranes with sub-1-nm pores show promise for ion/molecular separation, osmotic energy generation, and energy storage. Narrowing the pore size distribution and controlling the surface charge are essential to achieve these applications. However, nanoporous graphene membranes fabricated via conventional methods possess a broad pore size distribution and inadequately regulated surface charge, limiting their applications. Herein, we present a molecular anchoring approach for scalable synthesis of nanoporous graphene membranes via a bottom-up technique, aiming to narrow the pore size distribution without reducing the pore density while simultaneously adjusting the charge properties of nanopores. By selecting suitable anchoring molecules, the custom-tailored pore size distribution and chemical functionality of nanoporous graphene membranes can be achieved. Leveraging the steric restriction effect, anchoring monomers selectively traverse larger nanopores to form ion-selective plugs, effectively repairing these nanopores. The centimeter-scale nanoporous graphene membrane with an ion-selective plug achieves high separation selectivity ($K^+/Na^+=20$, $K^+/Mg^{2+}=330$). Theoretical simulations indicate that a smaller pore size, narrow pore size distribution, and positive charge result in a larger energy barrier difference, leading to ultrahigh metal ion selectivity. Furthermore, in treating lithium battery leaching solutions, Li^+/divalent ions selectivity exceeds 900. These findings provide a way for designing graphene-based membranes.

Membranes with angstrom-level ion selectivity and ultrahigh ion permeability are desirable for high-efficiency separation applications such as ion separation, gas separation, organic solvent nanofiltration, and electrochemical energy conversion and storage[1–5]. The latest advancements in membranes with pore sizes less than 1 nm have significantly enhanced ion sieving performance, sparking considerable research interest. Among these, commercially produced chemical vapor deposition (CVD) graphene, made via the roll-to-roll technique[6–8], has positioned atomically thin graphene membranes with angstrom-sized pores as leading candidates for ion separation owing to its atomic-scale thickness[9], enhanced mechanical integrity[10,11], and low flow resistance[12] to potentially transform the domain of traditional membrane-based separation technologies. Theoretical and experimental studies have demonstrated that nanoporous atomically

---

[1]Hubei Key Laboratory of Multi-media Pollution Cooperative Control in Yangtze Basin, School of Environmental Science & Engineering, Huazhong University of Science and Technology, Wuhan, Hubei 430074, China. [2]Department of Chemical Engineering, KU Leuven, Celestijnenlaan 200F, Heverlee 3001, Belgium. [3]Laboratory of Advanced Separations (LAS), École Polytechnique Fédérale de Lausanne (EPFL), Sion CH-1950, Switzerland. [4]Department of Chemical and Biological Engineering, Monash University, Clayton, Victoria, Australia. e-mail: pengrui.jin@kuleuven.be; yuanss@hust.edu.cn; huanting.wang@monash.edu

thin graphene membranes with uniform pores and a narrow size distribution outperform existing state–of-the-art liquid-phase membrane separation processes by orders of magnitude in terms of permeability and selectivity[2,13–15]. Nanopores can be introduced into atomically thin graphene by direct bottom-up fabrication or top-down post-etching methods such as plasma[16–19], ion bombardment[20,21], UV/ozone[22–25], and ion irradiation[3,26,27], with the drawback that not only the pore size distribution is a wide log-normal with long right tails but also the chemical functionality of the pores is poorly controlled[28]. Consequently, the presence of nonselective pores and cracks compromises the membrane selectivity, causing the experimental performance to fall short of the theoretical values from the molecular simulation[29–33].

To address the separation issues caused by non-selective pores and cracks, strategies for fabricating highly selective nanoporous graphene need to be pursued. One approach involves sealing large pores and cracks via interfacial polymerization (IP; this method is used to block leakage and then introduce pores via post-treatment) to mitigate their negative impact and create pores via post-treatment[27,34,35]. Additionally, creating an additional layer with Å-scale apertures, such as a polyelectrolyte coating or conjugated microporous polymer, can reduce the rapid, non-selective transport arising from nanoscale tears, cracks, and large non-selective pores in graphene, thereby increasing selectivity[24,36]. However, these methods increase the extra resistance and reduce the pore density, restricting water and ion transport and diminishing the benefits of using atom-thick graphene as the selective layer. In addition to steric hindrance, the control of electrostatic interactions between pores and ions is also important for improving membrane selectivity because of the different interaction energy barriers[37,38]. However, this aspect is challenging to achieve and has received less attention from the research community of monolayer porous graphene membranes because of their stable chemical properties.

Herein, we report a molecular anchoring technique that selectively patches large pores to confer ion-sieving properties to mitigate tailing effects without hindering subnanometer-selective pores. Moreover, the introduction of positively charged anchors results in a positive charge on the porous graphene membrane, facilitating the selective transport of mono-/multivalent cations and breaking the constraint imposed by the conventional log-normal size distribution. Unlike the previous IP-sealing methods[27,35], which completely block leaks and large pores, we introduce ion-selective plugs that repair leaks while imparting ion-selective properties. The prepared membrane exhibited highly efficient and precise mono-/multivalent separation. Molecular dynamics (MD) simulation calculations revealed that metal ion transport in graphene channels is associated with pore size distribution and pore charge–metal ion interactions, both of which contribute to a high barrier for divalent metal ions passing through the nanoporous graphene membrane and thus high mono-/divalent ion concentrations and mobility ratios in the membrane. We propose a strategy to increase the permeability and selectivity of porous graphene membranes, approaching their theoretical limits.

Results

Mechanically reinforced nanoporous graphene membranes

A large-area composite membrane with a mechanically reinforced nanoporous carbon (NPC) film and atomically thin nanoporous graphene was synthesized via one-step catalysis of Ni at low temperature, referred to as porous nanocrystalline graphene (PNG) [39] (Fig. 1a and Supplementary Fig. 1). During the preparation of the PNG membrane, the annealing of the nickel foil, the regulation of flatness and the verification of the precursor are very important for the synthesis of the PNG membrane (Supplementary Figs. 2–4, and the membrane preparation section for details). The NPC film strongly bonds with the nanoporous graphene[40], facilitating the incorporation of nanopores into the graphene structure with minimal tear and facilitating crack-free transfer. NPC films with a pore size of 20 nm (Fig. 1b and Supplementary Figs. 5a, b) and a thickness of 120 nm (Fig. 1b and Supplementary Fig. 5c) were formed, as observed via atomic force microscopy (AFM), scanning electron microscopy (SEM), and transmission electron microscopy (TEM). A nanoporous graphene layer is also formed[41]. Owing to the presence of the NPC layer in PNG, it is difficult to directly observe the distribution of pores in the graphene layer, so PNG2 (porous nanocrystalline graphene 2, see the membrane preparation section), containing only a graphene layer, was prepared for the observation of graphene pores. The addition of turanose will only bring about the NPC layer without affecting the formation of the graphene layer, so the pores of PNG and PNG2 in the graphene layer are the same[39]. Aberration-corrected high-resolution transmission electron microscopy (AC-HRTEM) revealed that nanoporous graphene has pores of varying sizes (Fig. 1c), with the most concentrated pore size being 1.3 nm from the statistics of the AC-HRTEM images (Fig. 1d, Supplementary Figs. 6a, 7 and Supplementary Note 1). Furthermore, selected-area electron diffraction (SAED) revealed a diffraction ring characteristic of graphene, confirming the successful synthesis of a large-area graphene structure (Supplementary Fig. 6b). The Raman spectrum clearly exhibited *D* and *G* peaks, whereas the weaker *2D* peak corresponded to the smaller grain size of nanocrystalline graphene (Fig. 1e). The *D* peak in the Raman spectrum, originating from the breathing of the six-atom ring in the graphene lattice, is activated by the presence of defects. Consequently, the I_D/I_G ratio can be used to calculate the defect density in graphene[24]. The calculated defect density was $4.8 \times 10^{11}\ \mathrm{cm}^{-2}$, closely approximating that of single-layer graphene treated with plasma[23] or ozone[40,42]. The pore size of the PNG was further determined by assessing the transmembrane conductance of chloride solutions containing tetramethyl, tetraethyl, tetrapropyl, and tetrabutyl chloride (Supplementary Fig. 8). The measurements revealed that the transmembrane mobility of the cations[43,44] (α_m) decreased as the hydration diameter of the cations increased. Using the hydrodynamic equation (Supplementary Note 2), the average pore size of the PNG membrane was estimated to be 1.38 nm, which agrees with the HRTEM results.

To make ion transport unrestricted and improve the mechanical strength of the membrane, the PNG was suspended on a Kevlar support[45]. The three-dimensional structure of Kevlar allows rapid ion transport and provides greater mechanical strength at the same time (Fig. 1a–f and Supplementary Figs. 9 and 10). The resulting suspended film was mechanically robust, as exemplified by the successful loading of weight (10 g) on top of the film (Supplementary Fig. 11). To test the transmission rate of PNG to various substances, a concentration-driven approach (using 0.1 M solution) was used to test the flux of different ions and molecules (Supplementary Figs. 12 and 13). The flux was in the range of 0.6–1.2 $\mathrm{mol/m^2/h}$ for different ions (Fig. 1g) and gradually decreased with increasing ion size. Furthermore, when the flux of tetracycline with a molecular size of approximately 1.4 nm was tested, the flux decreased sharply to 0.069 $\mathrm{mol/m^2/h}$ (Fig. 1g, h and Supplementary Fig. 14). On the basis of the flux of different ions and molecules, the Boltzmann equation[42] can be employed to determine the pore size distribution of PNG (Supplementary Fig. 15, Supplementary Note 3), which is consistent with the results obtained from the hydrodynamic equation and AC-HRTEM. In this process, the PNG membrane effectively separated NaCl and tetracycline, achieving a separation ratio exceeding 10 while maintaining high permeability to NaCl. These results suggest significant potential for the application of PNG membranes in the field of antibiotic desalination[46].

Size-dependent molecularly engineered PNG with tailored pore size and charge

Although the mechanical strength of nanoporous graphene membranes is reinforced by the NPC film and Kevlar substrate, the large pore size and obvious tailing effect on the pore size distribution of the

PNG membrane limit its application in biological K^+ nanochannels and mono-/divalent ion-selective devices. Karnik[27] and Zhang[35] developed a defect sealing strategy involving interfacial polymerization and the creation of selective pores via posttreatment to increase the selectivity of graphene membranes. The sealed graphene membranes were completely impermeable to ions such as K^+ and dye, demonstrating

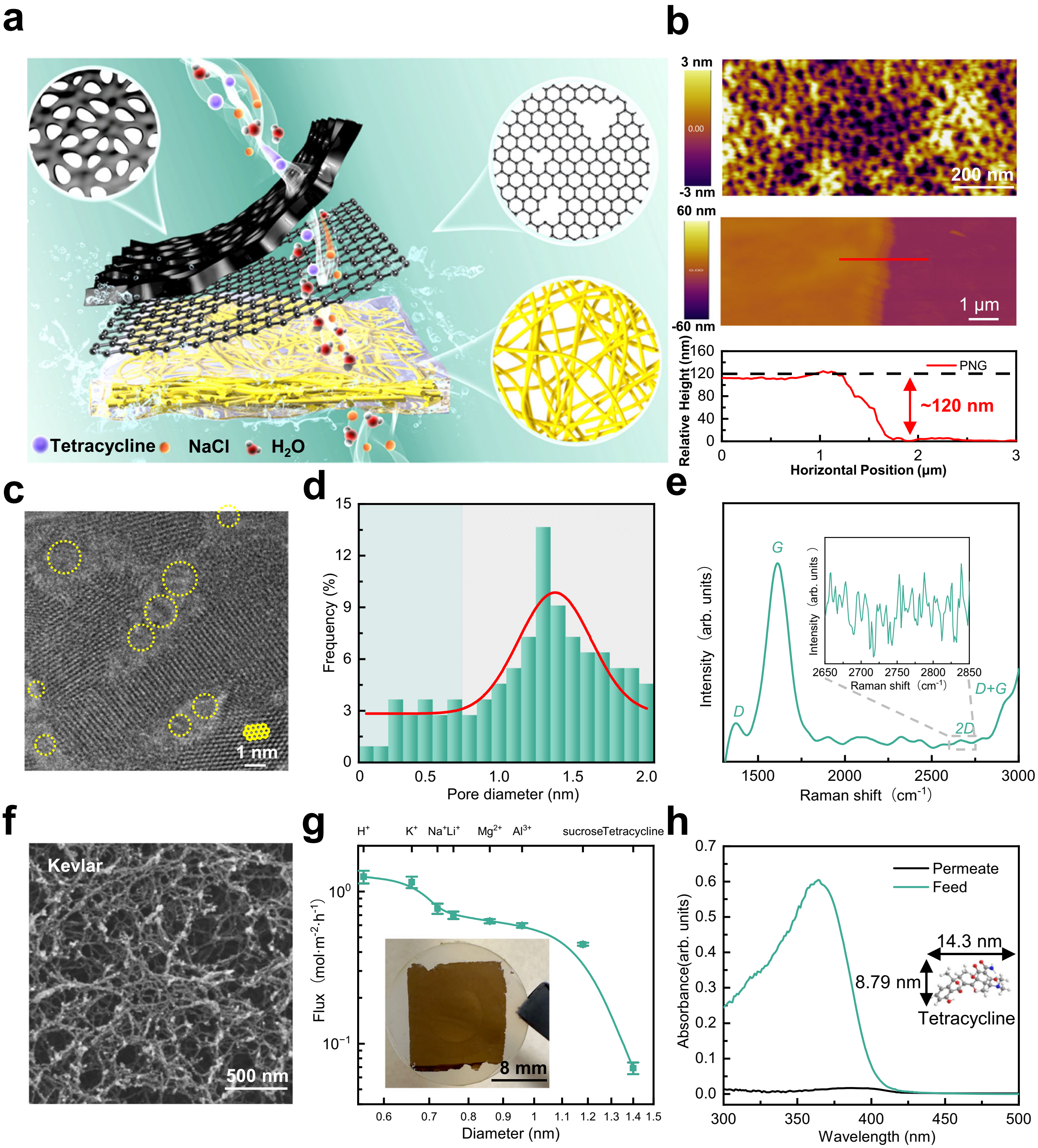

Fig. 1 | Fabrication and characterization of nanoporous graphene composite membranes. a Schematic diagram of the membrane structure, including the nanoporous carbon layer and nanoporous graphene, transferred to a Kevlar substrate for testing. **b** AFM images of the surface and cross-section of the PNG, showing the pore size of the NPC and the thickness of the PNG. **c** AC-HRTEM image of nanoporous graphene, the yellow circles represent the pores of the nanoporous graphene and the the yellow hexagon represents the crystal structure of graphene. **d** Pore size distribution of nanoporous graphene according to AC-HRTEM images, where selective and nonselective pores to K^+/Li^+ are highlighted in green and gray, respectively. **e** Raman spectrum of nanoporous graphene. The insets show the partially enlarged region from 2650 cm^{-1} to 2850 cm^{-1}. **f** SEM image of the Kevlar three-dimensional structure. **g** Flux of different ions and molecules for PNG; the inset shows a photo of the tested membrane, the error bar is the standard deviation from at least three samples, and the center of each error bar represents the average data from these samples. **h** UV–vis spectra of the feed and permeate solutions consisting of tetracycline dissolved in ethanol. The insets show the molecular structure of tetracycline.

great potential for desalination[22] and organic solvent nanofiltration applications. However, the reported interfacial polymerization methods significantly hinder mass transfer, and the improper selection of molecular size during interfacial polymerization results in poor selectivity between similarly sized ions such as K^+, Li^+, and Mg^{2+}. Inspired by the reported interfacial polymerization method, to simplify posttreatment and enhance the selectivity for ions of similar size at the same time, a size-dependent molecular anchoring strategy was developed involving the formation of plugs with an ion-selective aromatic network to repair nonselective tears and defects larger than the anchoring molecule, which concurrently introduces positive charges into the channels (Fig. 2a). Notably, the molecular anchoring in this case means that the anchoring molecule can only be anchored at graphene pores larger than its molecular size for reaction to form PA structures, due to the self-limitation of interfacial polymerization reaction and the difference of surface tension between water and oil, we speculate that PA plugs may be formed in the pores or outside of the pore which close to the oil phase side[22]. Piperazine (PIP)/polyethylenimine (PEI) and trimesoyl chloride (TMC) were added to the respective sides of the PNG membrane in two immiscible phases. The aqueous phase monomer (PIP, PEI) can react with molecules containing acyl chloride groups in the organic phase, forming ion-selective aromatic network plugs via interfacial polymerization[40] (Supplementary Fig. 16). Owing to its hydrophobicity and high reactivity with water, TMC largely remains in the organic phase and does not pass through large pores or defects into the aqueous phase. Consequently, only PIP/PEI molecules traverse pores or defects of the PNG membrane larger than its molecular size to reach the interface, and they subsequently react with TMC in the organic phase. Due to the self-limiting effect of interfacial polymerization[38,47,48], no complete PA layer structure can be formed[46,49,50], thereby forming ion-selective plugs that block all the nonselective leaky nanopores that are larger than the size of the PIP/PEI[38], owing to the different surface tensions, hydrogen bonding and π–π interactions between PIP/PEI molecules and the graphene membrane, the PA structure formed can remain stable at the graphene membrane pores (Supplementary Fig. 17). Therefore, the molecular size of the amine monomers (PIP, PEI) is the limiting factor of the reaction[48,51]. Specifically, PIP (Mw = 86), with a molecular size (0.70 nm) between that of the hydrated potassium ion (0.66 nm) and the hydrated lithium ion (0.76 nm) and featuring amino groups, confers positive charges to the channels[52]; thus, the reaction can only occur at pores or defects larger than 0.7 nm (Fig. 2a and Supplementary Table 1), which is expected to significantly narrow the pore size distribution and enhance the separation factor between potassium ions and lithium ions. Similarly, applying PEI (Mw = 600, 1.2 nm) as the amine anchor selectively blocked pores and defects larger than 1.2 nm. This demonstrates that specific adjustments in pore size and charge can be realized by selecting appropriate anchoring molecules (Fig. 2a). To eliminate the excess TMC hydrolyzed to form carboxyl groups in the oil phase and the electronegativity near the membrane pores, PIP/PEI was introduced to the oil phase to eliminate the possible electronegativity and strengthen the sealing effect. The unreacted amino groups on PIP/PEI can make the membrane pores appear positive. These further form ion-selective plugs at large tears and defects, reducing ion leakage. After molecular anchoring by PIP/PEI, the resulting membrane was referred to as MAP-PNG/MAE-PNG (where the P of MAP means PIP and the E of MAE means PEI).

To confirm the successful modification of the PNG membrane via size-dependent molecular anchoring technology, we characterized the changes in the surface functional groups of PNG and MAP-PNG/MAE-PNG. X-ray photoelectron spectroscopy (XPS) and attenuated total reflection infrared (ATR-IR) spectroscopy were performed after positioning the nanoporous graphene facing up (Supplementary Fig. 18). According to the XPS spectrum of PNG (Supplementary Fig. 19c), the proportion of N is relatively small, at approximately 2.8%, which is caused mainly by the small amount of N in the block copolymer[53], which was confirmed by the C=N and C≡N peaks in the fine spectrum of N 1*s* (Supplementary Fig. 19a). For MAP-PNG, the content of N on the membrane surface increased to 5.4% (Supplementary Fig. 19c, f), and obvious O=C−NH and $-NH_2$ groups were present (Supplementary Fig. 19a), indicating the successful molecular anchoring of PIP on PNG. The O=C−NH peaks in the fine N 1*s* spectrum of MAE-PNG (Supplementary Fig. 19b) also prove that PEI was molecularly anchored. The anchoring of PIP and PEI on PNG was further confirmed by the ATR-IR results (Supplementary Fig. 20). The weak −OH peak at 3300–3500 cm^{-1} in the spectra of MAP-PNG and MAE-PNG were enhanced and sharp, and absorption peaks corresponding to C=O and C−N appeared at 1660 cm^{-1} and 1546 cm^{-1}, indicating the successful grafting of amino groups on the membrane surface. The relatively larger hydrophilic and positive areas of MAP-PNG resulted in lower water contact angles and greater positive potentials (39.7° and 660 mV, respectively) than those of PNG (75.6° and −170 mV, respectively) and MAE-PNG (64.7° and 370 mV, respectively) (Fig. 2b, Supplementary Fig. 21). The enhanced positive charge facilitates the selectivity of mono-/multivalent cation separation.

Furthermore, the total N content in MAP-PNG (5.4%) and MAE-PNG (3.8%) is much lower than that of the complete traditional PA selective layer (~15%)[38,48] resulting from traditional interfacial polymerization, indicating that molecular anchoring only occurs at the defect area rather than forming a complete layer. The positions for molecular anchoring are mainly determined by the randomly distributed larger pores and defects in the PNG, which lead to a nonuniform N distribution across the membrane. This was confirmed by energy dispersive spectroscopy (EDS) mapping (Supplementary Fig. 22). In addition, compared with that in the MAE-PNG membrane (3.8%), the relatively higher content of N in the MAP-PNG membrane (5.5%) indicates that the PIP molecular anchoring reaction occurs in more locations and areas because the number of defects and pores larger than 0.7 nm is greater than that of defects and pores larger than 1.2 nm. In addition, atomic force microscope infrared spectroscopy (AFM-IR) was used to detect the distribution of functional groups on the membrane surface at the nanoscale (Fig. 2d). The preparation of the AFM-IR sample is shown in Supplementary Fig. 18. In contrast, the original PNG membrane (Supplementary Fig. 23a (2)) did not have the characteristic peak corresponding to the amide bond at 1580 cm^{-1}, whereas the surface of the MAP-PNG (Fig. 3e (2)) and MAE-PNG (Supplementary Fig. 23a (6)) membranes presented an uneven distribution of the characteristic peak of the amide bond compared with that of the membrane with the PIP/TMC membrane (Supplementary Fig. 23a (4)), which presented an even distribution of the characteristic peak of the amide bond. The uneven distribution indicates that no complete PA layer is formed in the MAP-PNG and MAE-PNG membranes, but only an IP plug is formed in the large graphene membrane pores. Six locations (Fig. 3f and Supplementary Fig. 23b) of the four membranes were scanned from 1400 cm^{-1} to 1700 cm^{-1}. For locations with PA structures, peaks corresponding to C−N, C−N + N−H, N−H, and C=O bonds appeared at 1410 cm^{-1}, 1490 cm^{-1}, 1580 cm^{-1}, and 1660 cm^{-1}, respectively. This finding also shows that the PA structure is not evenly distributed on the surface of the MAP-PNG and MAE-PNG membranes, indicating that the IP reaction only occurs in the larger pore position. At the same time, due to the limit of monitoring accuracy and the large pore density, some PA structures may be close to each other, resulting in the formation of large discontinuous PA structures (close to 100 nm) in the characterization process. A relatively large number of defects and pores normally results in a high molecular diffusion rate across a nanoporous graphene membrane. To experimentally demonstrate this, the diffusion rates of PIP and PEI across the PNG membrane were compared in a concentration-driven cell device. The diffusion rate of PIP in PNG was approximately 20 times faster than that of PEI (Supplementary Figs. 24 and 25). By testing cross sections of the PNG, MAP-

PNG and MAE-PNG composite membranes, the thickness of the membranes did not significantly change after molecular anchoring, but the surface of the membranes became rougher according to AFM characterization, which also revealed the uneven distribution of the PA structure (Supplementary Figs. 26 and 27). The differences of the AFM-IR, AFM maps, and EDS data can be attributed to the distinct spatial resolutions and contrast mechanisms inherent to each characterization method.

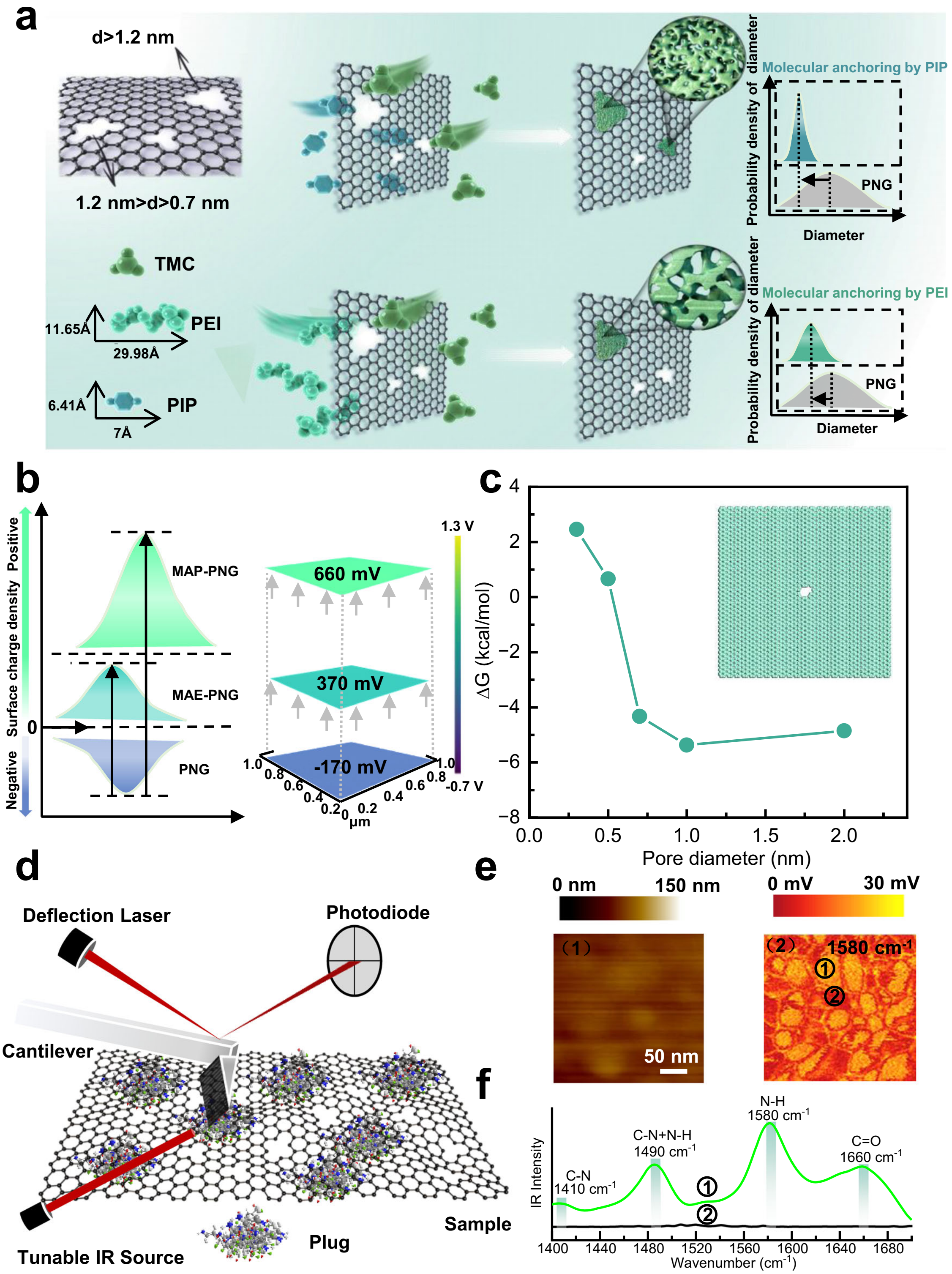

Fig. 2 | Size-dependent molecularly engineered PNG with tailored pore sizes and charges. a Schematic diagram of the molecular anchoring of different molecules to PNG membranes with different pore sizes. **b** Schematic diagram of charge adjustment after anchoring PNG membrane molecules with PIP and PEI and the potentials of PNG, MAE-PNG, and MAP-PNG measured via KPFM. **c** The free energy difference Δ*G* between trimesoyl chloride and piperazine molecules surrounding single pores of different sizes; inset: a representative 1 nm nanopore etched on single-layer graphene. **d** AFM-IR test principle concept diagram, which includes a deflection laser transmitter, a photodiode, an IR source and a needle tip probe. **e** Surface morphology from AFM (1) and infrared absorption spectra at 1580 cm^{-1} for the MAP-PNG membrane (2). **f** Spectrum of the infrared absorption at positions 1 and 2 from 1400 cm^{-1} to 1700 cm^{-1}.

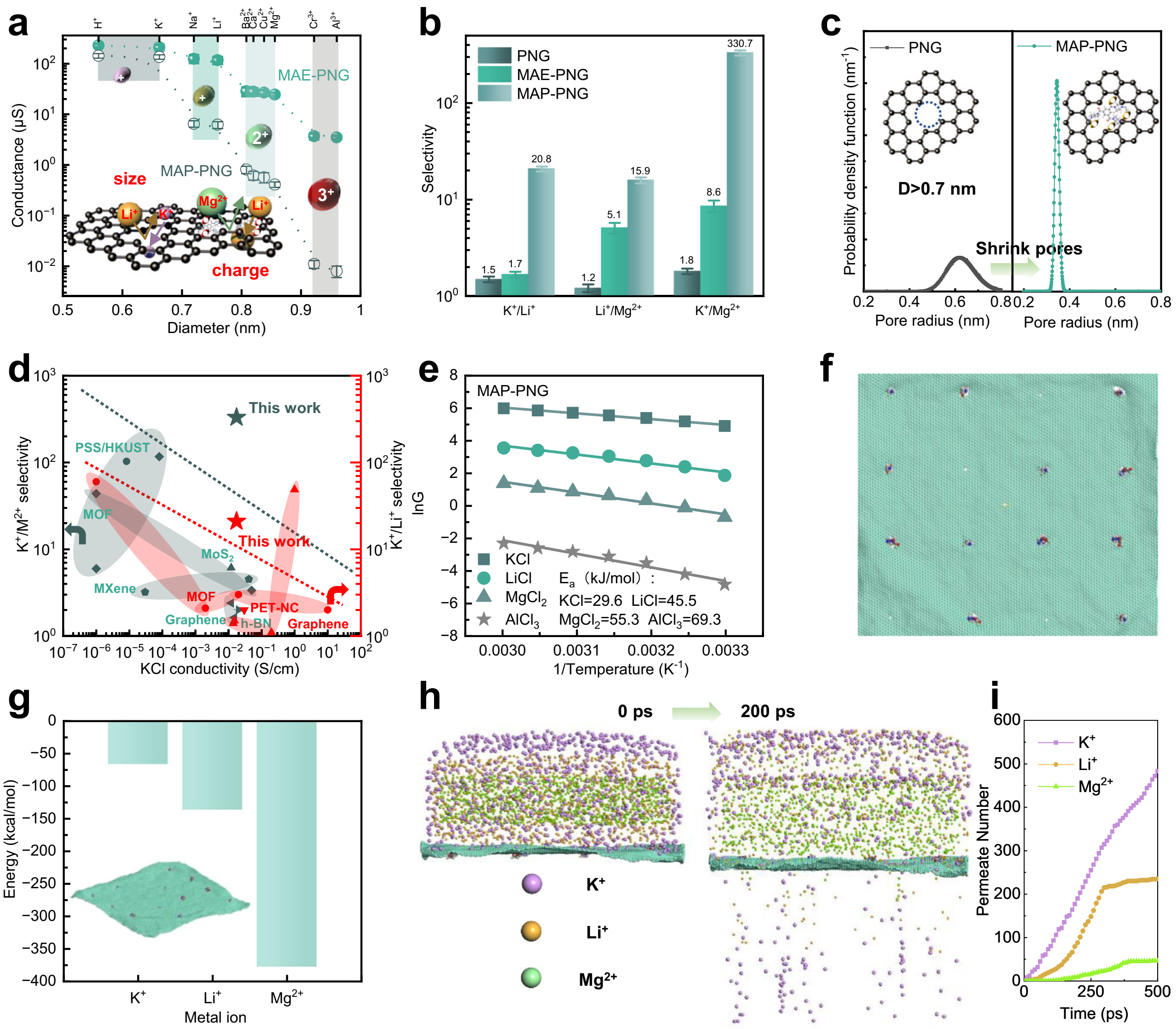

Fig. 3 | Performance of nanoporous graphene membranes. a Ionic conductance of MAP-PNG and MAE-PNG measured in 0.1 M chloride salt solutions at −1 V, the error bar is the standard deviation from at least three samples, and the center of each error bar represents the average data from these samples; inset: schematic diagram of the separation principle by size and charge; **b** selectivity of PNG, MAP-PNG and MAE-PNG between K^+, Li^+ and Mg^{2+}, the error bar is the standard deviation from at least three samples, and the center of each error bar represents the average data from these samples; **c** pore size distribution of PNG and MAP-PNG; inset: schematic diagram of pore size and charge change; **d** comparison of the membrane performance using a single solution reported in the literature, where the gray background represents K^+/M^{2+} (0.1 mol/L KCl and 0.1 mol/L M^{2+}) selectivity and the red background represents K^+/Li^+ (0.1 mol/L KCl and 0.1 mol/L LiCl) selectivity. The red and gray lines are added to highlight the trade-off between ion conductivity and ion-ion selectivity. **e** Transmembrane energy barriers of MAP-PNG for KCl, LiCl, $MgCl_2$, and $AlCl_3$. **f** Model of MAP-PNG for different ions across the membrane. **g** Transmembrane energies of K^+, Li^+, and Mg^{2+} for MAP-PNG; **h** initial model state and after 200 ns of the permeation process; **i** the number of K^+, Li^+, and Mg^{2+} ions that permeated across the MAP-PNG after 500 ps.

The above chemical analyses revealed that the molecular anchoring reaction is significantly influenced by the size of the amine monomers and the pores of the PNG. To determine whether anchoring is sterically governed by the size of the pores and PIP, the Gibbs free energy of the reaction at different single pore sizes was calculated (Supplementary Fig. 28). The free energy difference ΔG was determined via MD simulations between two specific scenarios: (i) with two unreacted molecules on opposite sides of a pore and ii) with the molecules reacting to form new bonds across the pore. The computed $|\Delta G|$ is close to 0 kcal/mol for pores less than 0.7 nm but increases to ~5 kcal/mol for larger pores (Fig. 2c), indicating that anchoring is favorable only for pores larger than the monomer.

Molecularly anchored nanoporous graphene membranes for precise sieving

Ion diffusion experiments using MAP-PNG and MAE-PNG validated the effectiveness of the molecular anchoring strategy. The voltage and current curves of different ions under electric field-driven conditions were obtained, and their conductance was calculated to evaluate their ion separation performance (Fig. 3a and Supplementary Fig. 29). The selectivity of K^+/Li^+ slightly increased from 1.5 to 1.7 after the PNG was molecularly anchored by PEI (1.20 nm), which has a molecular size much larger than that of hydrated potassium ions (0.66 nm) and hydrated lithium ions (0.76 nm) (Fig. 3b). This is primarily due to the relatively large size of PEI, which cannot block the nonselective pores for K^+ and Li^+ with sizes between 0.76 nm and 1.2 nm. In contrast, modifying PNG with PIP (0.70 nm), whose molecular size falls between those of the hydrated potassium ions and hydrated lithium ions, results in a significantly higher K^+/Li^+ selectivity of 20.8, mainly because all the nonselective pores for K^+ and Li^+ were plugged. This confirms that the pore size distribution of PNG can be intentionally narrowed for specific separation by using proper anchors of the right size, which aligns with our expectations. In terms of the separation between Li^+ and Mg^{2+}, the molecular size of PIP (0.7 nm) is smaller than the hydrated diameters of Li^+ (0.76 nm) and Mg^{2+} (0.92 nm), whereas the molecular size of PEI (1.2 nm) exceeds the hydrated diameters of Li^+ (0.76 nm) and Mg^{2+} (0.92 nm). Consequently, MAP-PNG and MAE-PNG cannot be separated through size exclusion alone. However, owing to their differing positive charges, Li^+ and Mg^{2+} experience varying electrostatic repulsion with the highly positively charged MAP-PNG membrane, thus resulting in a separation ratio between Li^+ and Mg^{2+} of 15.9, whereas MAE-PNG, with a relatively low positive charge (Fig. 2c), leads to a comparatively poor separation ratio of 5.1 (Fig. 3b). In the separation of K^+ and Mg^{2+}, the MAP-PNG membrane effectively separated K^+ and Mg^{2+} ions through a synergistic combination of size exclusion and charge effects. This is due to the relatively high positive charge, as well as the fact that the molecular size of PIP (0.70 nm) is larger than the hydrated diameter of K^+ (0.66 nm) but smaller than that of Mg^{2+} (0.76 nm). As a result, a separation ratio of up to 330 was achieved (Fig. 3b). Compared with the separation performance reported in similar fields, MAP-PNG showed superior performance to other state-of-the-art membranes in terms of mono/monovalent (K^+/Li^+) selectivity and mono/multivalent ion (K^+/M^{2+}) separation (Fig. 3d, Supplementary Note 4, Supplementary Tables 2 and 3). In addition, the Boltzmann equation was used to fit the conductance curves of various solutes to reveal the pore size distribution of MAP-PNG. According to the fitting results (Supplementary Fig. 30), molecular anchoring with PIP significantly reduces the tailing effect on the pore size distribution (Fig. 3c). The pore size of the MAE-PNG was further determined by assessing the transmembrane conductance of chloride solutions containing tetramethyl, tetraethyl, tetrapropyl, and tetrabutyl chloride via the same method used for the measurement of PNG pore size (Supplementary Fig. 31). The average pore size of the MAE-PNG membrane was estimated to be 1.2 nm, which agrees with the design results. Furthermore, in an extended K^+, Li^+ and Mg^{2+} mixture separation experiment spanning 4 days, stable ion flux and high selectivity were observed (Supplementary Fig. 32), indicating the robustness of the graphene membrane. The fluxes of K^+, Li^+, and Mg^{2+} in the PNG membrane are all ~0.1 mol/m^2/h (Supplementary Fig. 32). The mono-/bivalent selectivity is slightly greater than that of the single salt test. Compared with that of the PNG membrane, the flux of the MAP-PNG membrane decreased slightly because of the selective plugging of the nonselective large pores of the porous graphene. Furthermore, the K^+/Mg^{2+} selectivity increased from 330 to more than 600 compared with the results from the single salt test. In addition, for comparison, we prepared PIP-TMC and PEI-TMC membranes on Kevlar substrates and tested their performance for ion separation. The results show that the PIP/PEI-TMC membranes essentially do not show monovalent/bivalent cation selectivity or monovalent/monovalent cation selectivity (Supplementary Fig. 33).

To further elucidate the transport mechanism of different ions in MAP-PNG, the energy barrier of different ions crossing the membrane and the ion concentration distribution during transmembrane transport were investigated via experimental tests and computational simulation. The linear relationship between conductance and temperature was obtained according to the Arrhenius formula for MAP-PNG (Fig. 3e) and MAE-PNG (Supplementary Fig. 34), which can be further calculated to obtain the activation energy of different ions (Supplementary Note 5). The significant differences in activation energy for K^+ (29.6 kJ/mol), Li^+ (45.5 kJ/mol), Mg^{2+} (55.3 kJ/mol), and Al^{3+} (69.3 kJ/mol) align well with the selectivity of MAP-PNG for different ions. For the MAE-PNG membrane, the similar activation energies for K^+ (21.2 kJ/mol) and Li^+ (25.9 kJ/mol) are consistent with its relatively low selectivity for K^+ and Li^+. Compared with those of K^+ and Li^+, the activation energies of Mg^{2+} (37.8 kJ/mol) and Al^{3+} (49.5 kJ/mol) are greater, confirming their high selectivity for mono-/multivalent ions.

Moreover, to verify the theoretical accuracy of the experimental results at the molecular level, MD simulations were used to simulate the transmembrane processes of different ions. K^+, Li^+, and Mg^{2+} were placed on top of the graphene layer (Supplementary Fig. 35). The reacted molecules, which serve as ion-selective plugs, were placed around pores with diameters larger than 0.7 nm in the porous graphene (Fig. 3f). The energy required for ions to traverse these pores was calculated on the basis of the difference in energy before and after permeation. The results (Fig. 3g) reveal an obviously greater energy barrier for Mg^{2+} than for K^+, indicating that K^+ permeates the membrane more easily than does Mg^{2+}. This resulted in the significant selectivity of MAP-PNG for K^+ over Mg^{2+}. Finally, we simulated the ion concentration distributions of different ions on both sides of the membrane over time (Fig. 3h and Supplementary Fig. 36). K^+ permeated through MAP-PNG at a constant rate; regardless of spatial limitations, Li^+ permeated less than K^+, and Mg^{2+} did not permeate the membrane at all (Fig. 3i). These findings theoretically confirm that MAP-PNG can serve as a biological K^+ nanochannel by conducting K^+ much more rapidly than other ions with K^+/Na^+ selectivity up to approximately 20 and mono-/divalent ion-selective devices by impeding the transport of most divalent cations.

Practical lithium recovery from spent lithium-ion batteries

To demonstrate the potential for practical application of the MAP-PNG membrane in the industry, the separation performance of MAP-PNG was tested via lithium-ion battery leaching solutions. In step 1, a PNG membrane can effectively remove large molecules to obtain a high-concentration metal-rich ion solution that contains Li^+, Ni^{2+}, Co^{2+}, and Mn^{2+} (Fig. 4a). In step 2, as the pore size of MAP-PNG decreased and a positive charge was introduced, effective separation of Li and other divalent cations was achieved by the MAP-PNG membrane. Furthermore, we demonstrated the scalability of the membrane by preparing a centimeter-level composite membrane (Fig. 4b) and successfully transferred it to the Kevlar-based membrane to form a composite membrane with good flexibility that can be bent at will (Fig. 4c and Supplementary Fig. 37), which verified the scalability and mechanical flexibility of the membrane, and the superiority of the membrane area was presented along with a comparison with reported state-of-the-art membranes (Supplementary Fig. 38 and Supplementary Table 4). For the filtration of lithium battery leaching solutions, a simulated battery leaching solution was prepared[54], mainly containing Li^+, Co^{2+}, Ni^{2+}, Mn^{2+}, and SO_4^{2-} ions, with the pH adjusted to 2 via sulfuric acid due to actual leaching in industry. Sulfuric acid is usually used to leach the cathode material of waste lithium-ion batteries. The flux of Li^+ was 0.021 mol/m^2/h, whereas the fluxes of Co^{2+}, Ni^{2+}, and Mn^{2+} were as low as 10^{-5} mol/m^2/h, as Li^+ is different from other divalent cations in terms of its hydrated radius and charge, resulting in the selectivity of Li^+ to divalent ions exceeding 900 (Fig. 4d). Moreover, we also used a hydrochloric acid system to test the effects of different anions on the membrane separation performance, and the results revealed that different anions had little effect on the membrane separation

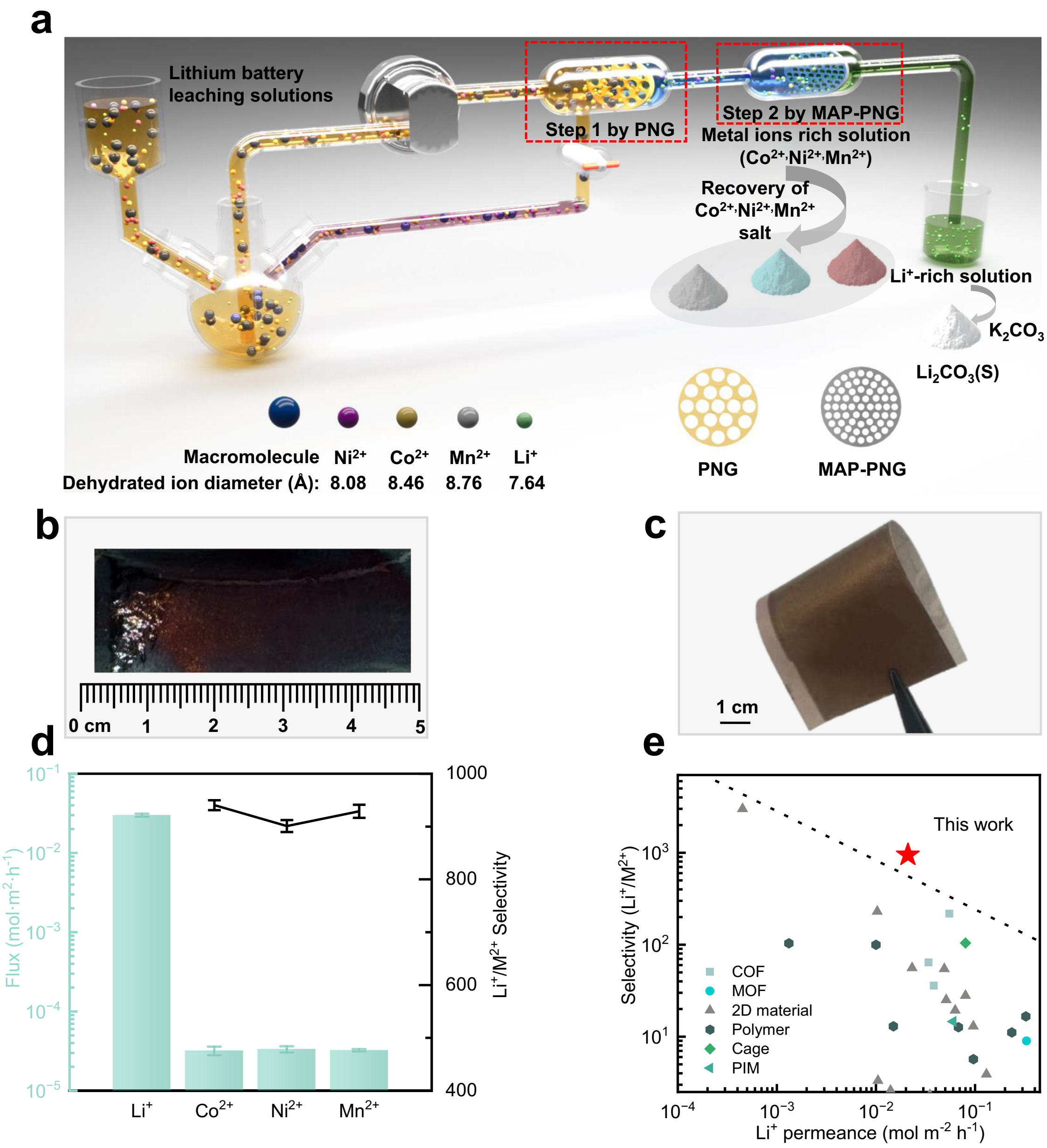

Fig. 4 | Scalability and practical application of nanoporous graphene membranes in treating spent lithium-ion battery leaching solutions. **a** Recovery of lithium and metal salts from lithium-ion battery leaching solutions via PNG and MAP-PNG membranes. **b** The centimeter scale of MAP-PNG, **c** the flexibility of the MAP-PNG membrane, **d** the ion transport rate and selectivity of MAP-PNG in treating simulated lithium battery wastewater, the error bar is the standard deviation from at least three samples, and the center of each error bar represents the average data from these samples, and **e** a comparison of the Li^+/M^{2+} selectivity and Li^+ permeance for MAP-PNG and other membranes. A black line is added to highlight the trade-off between the ion permeance and ion–ion selectivity.

performance (Supplementary Fig. 39). The rapid transport of Li^+ and high selectivity of Li^+ over divalent ions enable the MAP-PNG membrane to effectively concentrate Li^+ from the lithium battery leaching solution, yielding a high-purity Li^+-containing solution and facilitating efficient recovery and reuse of Li^+. The enriched high-value metal ions (Co^{2+}, Ni^{2+}, and Mn^{2+}) can also be recovered via further treatment. Furthermore, the successful treatment of lithium battery leaching solutions demonstrated that the membrane has good acid resistance, highlighting the application potential of MAP-PNG under harsh conditions.

In summary, the ion-sieving performance of MAP-PNG surpasses that of most reported state-of-the-art ion-sieving membranes (Fig. 4e and Supplementary Table 5), such as covalent organic frameworks (COFs), metal organic frameworks (MOFs), 2D materials (graphene and MXenes), polymers with intrinsic microporosity (PIMs), and commercially available polymer membranes and cages. Compared with the state-of-the-art ion-sieving membrane, MAP-PNG has excellent selectivity for Li^+/M^{2+} and facilitates the flux of lithium ions, which indicates its potential to overcome the trade-off between selectivity and flux.

Discussion

We demonstrated the efficient fabrication of large-area nanoporous atomically thin graphene membranes with narrow pore size distributions and positive charges via a bottom-up molecular anchoring approach. By choosing an appropriate anchoring monomer, graphene pores and leaks larger than 0.7 nm could be repaired with ion-selective plugs, narrowing the pore size distribution with ultrasmall tail deviation at the Å scale. In addition, anchoring amino groups to nanopores on graphene during this molecular engineering process enhances the precise sieving of cations with different valence states. High monovalent ion flux combined with outstanding ion selectivity in mono/monovalent (K^+/Li^+ separation factor of 21) and mono/multivalent separations (K^+/Mg^{2+} separation factor of 330, Li^+/divalent ion separation factor exceeding 900) surpassed the performance of previously reported materials. Large-area monolayer nanoporous graphene with scalability and mechanical flexibility is excellent for recovering high-purity lithium from acid lithium battery leaching liquid, highlighting its promising application in resource recovery. The molecular engineering approach presented in this work allows for precise customization of the pore size distribution and charge properties, which provides a platform technology that enables control over the pore size and charge density for creating tailored monolayer nanoporous graphene membranes.

Methods

The detailed methods are described in the Supplementary Information.

Chemicals

Poly(styrene)-B-poly(4-vinylpyridine) (PS-b-P4VP) (Mw/Mn = 1.08) was purchased from Polymer Source. D-Turanose, ethylene imine polymer (PEI), and tetracycline were purchased from Macklin. Ni foil (99.9%, 0.025 mm) was purchased from Good Fellow. Piperazine (PIP) and 1,3,5-benzenetricarboxylic acid chloride (TMC) were purchased from Aladdin. Acetone (AR), isopropanol (AR), dimethyl sulfoxide (DMSO, AR), N,N-dimethylformamide (DMF, AR), and hexane (AR) were purchased from Sinopharm Chemical Reagent Co., Ltd. $FeCl_3$ (98%) was purchased from J&K Scientific. Kevlar aramid fibers were purchased from Thread Exchange. All the chemicals were used without further purification.

Membrane preparation

As shown in Supplementary Fig. 1, a PNG thin film is a type of product that is formed by pyrolysis in a tube furnace using the former copolymer and turanose as precursors. In brief, the preparation of the film mainly included annealing the nickel foil, polishing, synthesis of the casting solution, spin coating and pyrolysis. First, the nickel foil was annealed in a CO_2/H_2 atmosphere for 2 h. Subsequently, the nickel foil was polished and washed with acetone and isopropanol; only after annealing and polishing did the nickel sheet become crystalline, and the surface became flatter, resulting in the formation of a graphene membrane (Supplementary Fig. 2). The casting solution was composed mainly of PS-b-P4VP and turanose and was dissolved in a DMF solution. Specifically, 0.1 g of PS-b-P4VP and 0.2 g of turanose were dissolved in 2 g of DMF, and ultrasonic treatment was carried out for 90 min. The casting liquids of PNG and PNG2 (without turanose) were obviously different in the optical images. The PNG casting solution was a thick black liquid, whereas the PNG2 casting solution was a transparent liquid (Supplementary Fig. 3). Then, the solution was heat-treated at 180 °C for 3 h in a reaction kettle, and the casting solution was spin-coated on the annealed nickel foil (1000 rpm for 30 s and 1500 rpm for 30 s). The nickel foil covered with the casting solution was subsequently pyrolyzed in a tube furnace at 500 °C for 1 h and then quickly cooled to room temperature. Thermogravimetric analysis was used to test the weight loss of the raw material and the PNG film precursor under the same heating procedure, demonstrating the successful synthesis of the casting film solution (Supplementary Fig. 4). Then, the Kevlar layer was spin coated (1000 rpm for 60 s) on the surface of the PNG film to further increase the mechanical strength of the PNG film and reduce the introduction of transfer process defects. The resulting PNG/Ni was floated on a 1 M $FeCl_3$ bath to etch the Ni foil. Once the etching was complete, the floating PNG film was rinsed in a 1 M HCl solution and deionized water to remove the residues. Finally, the PNG was scooped on the as-prepared Kevlar substrate membrane (the Kevlar bulk fiber was dissolved in DMSO containing KOH and then cast onto a glass plate, and phase inversion in deionized water was used to obtain a Kevlar membrane). After air drying, the resulting PNG/Kevlar composite membrane was mounted on an H-cell device, and degassed PIP/PEI aqueous solution (0.2 wt%) was added to the nanoporous graphene side for 10 min and then poured out. Next, a TMC solution (0.15 wt%) in hexane was added to the Kevlar side by a glass dropper to allow IP for 10 min, and then, a PIP/PEI aqueous solution (0.2 wt%) was added to the Kevlar side to eliminate the residual TMC. The composite membrane was subsequently washed five times with deionized water and ethanol and then air dried for testing and characterization.

Characterization methods

Scanning electron microscopy (SEM) images of the surface and cross-sections of the PNG films were obtained on a TESCAN MIRA LMS scanning electron microscope operating at 3 kV. Atomic force microscopy (AFM) and Kelvin probe force microscopy (KPFM) images were recorded on a Bruker Dimension Icon AFM instrument. The thicknesses of the PNG and substrate were measured via AFM. The potentials of PNG, MAE-PNG, and MAP-PNG were measured via KPFM.

Raman spectroscopy—PNG films were transferred without a reinforcement layer onto a SiO_2/Si wafer for Raman characterization. Briefly, the Ni substrate was etched in a 1 M $FeCl_3$ solution, and the floating PNG film was washed with 1 M HCl and water and then rinsed with a Si wafer. Raman spectra were collected by using a LabRAM HR800 ($\lambda_L = 532$ nm) from the Horiba Jobin Yvon Company.

Attenuated total reflection infrared (ATR-IR) spectroscopy—changes in the functional groups of the PNG, MAP-PNG and MAE-PNG films were detected with a Nicolet iS50R instrument from Thermo Scientific. X-ray photoelectron spectroscopy (XPS)—the functional groups of the PNG, MAP-PNG, and MAE-PNG films were detected on a Thermo Kalpha instrument. For the ATR-IR and XPS analyses, the PNG membrane was transferred to the PES substrate for molecular anchoring, the PES was dissolved by NMR, and the nanoporous graphene side was opened (Supplementary Fig. 17).

Transmission electron microscopy (TEM)—nanoporous membranes were directly transferred to a copper grid and imaged. Briefly, the PNG films were transferred without any reinforcement by (i) etching the Ni foil in a 1 M $FeCl_3$ bath; (ii) floating the freestanding PNG film in a 1 M HCl bath for 1 h and then in a deionized water bath for 1 h to remove residues from the etching bath; (iii) fishing the floating film using a copper TEM grid; (iv) drying at room temperature for at least 12 h; and (v) imaging without any cleaning treatment. Aberration-corrected high-resolution transmission electron microscopy (AC-HRTEM) images of graphene were obtained with a JEOL JEM ARM200F instrument. The incident electron beam was monochromated ("rainbow" mode illumination) to reduce the effects of chromatic aberration, and a negative spherical aberration (Cs) of ~20 μm and slight overfocus was used to give a "bright atom" contrast in the images. An 80 keV incident electron beam was used for all the experiments to reduce electron radiation damage. The dose rate was maintained at $\sim 2 \times 10^4\ e^- s^{-1}\ Å^{-2}$ during imaging, and a slit was used to expose only the area of the sample being imaged to the electron beam. To obtain a typical PNG image, the targeted area was exposed to $\sim 2 \times 10^5\ e^- Å^{-2}$ during focusing and imaging. Continuous images with a 200 ms exposure were taken, and the first 5–10 frames (each frame corresponds to a dose of approximately $4 \times 10^3\ e^- Å^{-2}$) were integrated into the final image. Owing to the existence of the NPC film, it is difficult to directly observe the nanoporous graphene structure from the PNG membrane, so we synthesized a membrane containing only nanoporous graphene, which is referred to as PNG2. The synthesis of PNG2 was similar to that of PNG, but the main difference lies in the casting solution. For the PNG2 casting solution, 0.25 g of PS-b-P4VP was dissolved in 2 g of DMF, followed by ultrasonic treatment for 90 min without heat treatment, and the other steps were the same as those for PNG.

Inductively coupled plasma optical emission spectrometer (ICP–OES)—the concentration of ions was detected by a Prodigy Plus from the Leeman Labs Company.

Thermogravimetric analysis (TGA)—the variations in the quality of the raw materials with temperature were recorded by a Pyris1 TGA instrument from PerkinElmer Instruments. The heating procedure is completely consistent with the pyrolysis process. Under a nitrogen atmosphere, the temperature was increased from room temperature to 500 °C at a rate of 1 °C/min, after which the temperature was maintained for 1 h, after which the quality change was recorded.

Concentration-driven single salt transport measurements

For the diffusion test, a bilateral diffusion cell was used, and different salts were used as solutes. The effective membrane diameter was 8 mm. First, the membrane was installed on the osmotic tank, wetted with an ethanol/H_2O mixture (50 wt%) on both sides of the diffuse cells for 5 min, and then replaced with deionized water 3 times. Then, 50 ml of different salt solutions (0.1 M) was added to the feed pool facing the selective layer, 50 ml of deionized water was added to the permeate side facing the basement membrane, and the concentration of different salts on the permeate side was monitored in real time with a conductivity meter. All diffusion tests were stabilized for 30 min before data collection, and the solutions on both sides were stirred at 1500 rpm. The flux of the solute is calculated according to equation[27]:

$$J = \frac{V}{S} * \frac{\mathrm{dc}}{\mathrm{dt}} \tag{1}$$

where J is the flux, V is the feed volume, $\mathrm{d}C/\mathrm{d}t$ is the slope of the osmotic concentration as a function of time, and S is the effective membrane area.

The selectivity, S_{ij}, of one cation, i, over another, j, was calculated as:

$$S_{ij} = \frac{J_i}{J_j} \tag{2}$$

where J_i is the flux of cation i.

Mixed-salt transport measurements

For the transport test of mixed salt, the same device used for the single salt test was used. Then, 50 ml of KCl/LiCl/$MgCl_2$ solution (0.1 M) was added to the feed pool facing the selective layer, 50 ml of deionized water was added to the permeate side facing the basement membrane, and the concentrations of different salts on the permeate side were tested via ICP–OES. The solutions on both sides were stirred at 1500 rpm. The diffusion permeability of the solute was calculated according to the following equation:

$$J = \frac{\Delta C}{S^* \Delta T} \tag{3}$$

where C is the solute concentration difference of the permeate side, S is the effective membrane area, and T is the time of the test.

The selectivity, S_{ij}, of one cation, i, over another, j, was calculated as:

$$S_{ij} = \frac{J_i}{J_j} \tag{4}$$

where J_i is the flux of cation i.

Selective ion transport properties by linear sweep voltammetry (LSV)

The ion transport behavior of the different membranes was monitored by linear sweep voltammetry (LSV) using an identical ionic strength of 0.1 M for all tested single-electrolyte solutions in a laboratory-scale electrodialysis cell. The electric potential was swept from −1 V to +1 V at a rate of 5 mV s^{-1}, and the response was recorded. The membrane device was sandwiched between two reservoirs containing a single-electrolyte solution. Silver/silver chloride electrodes were separately fixed in two reservoirs for all I–V measurements[55].

For quantitative comparison, the ion selectivity ratios of the metal ions were calculated as the ratio of the measured conductance of the membrane for various cations according to the following Eq. (5), taking into consideration the valence difference:

$$\text{ion selectivity ratio} = \frac{Z_j}{Z_i} * \frac{G_\mathrm{i}}{G_j} \tag{5}$$

where ionic conductance (G_i and G_j) of membranes is the ratio of the current to the corresponding voltage in an electric drive measured in 0.1 M chloride salt solutions at −1 V or +1 V, respectively, at the same concentration; where Z_i and Z_j are the charge valences of the cations.

Lithium battery leaching solution treatment measurements

For the transport test of the lithium battery leaching solution, the same device used for the single salt test was used. Then, 50 ml (Li^+: 0.3 M; Co^{2+}/Ni^{2+}/Mn^{2+}: 0.001 M) of solution was added to the feed pool facing the selective layer, the pH of the solution was adjusted to 2 by H_2SO_4, 50 ml of deionized water was added to the permeate side facing the basement membrane, and the concentration of different salts on the permeate side was tested via ICP–OES. The solutions on both sides were stirred at 1500 rpm. The diffusion permeability of the solute was calculated according to the following equation:

$$J = \frac{\Delta C}{S^* \Delta T} \tag{6}$$

where C is the solute concentration difference of the permeate side, S is the effective membrane area, and T is the time of the test.

The selectivity, S_{ij}, of one cation, i, over another, j, was calculated as:

$$S_{ij} = \frac{J_i}{J_j} \tag{7}$$

where J_i is the flux of cation i.

Molecular dynamics (MD) simulations

All the molecular dynamics (MD) simulations were performed via Materials Studio. In this study, a graphene sheet with a size of 9.85 nm × 9.85 nm in the x–y plane was built. The pores were created by deleting atoms from random circular areas with various diameters ranging from 0.3 nm to 3 nm in pristine graphene. For porous graphene containing several pores with an average diameter of 0.7 nm, the pore size and distribution were designed to eliminate the effects of the defect concentration and boundaries. Periodic boundary conditions were applied in the x and y directions, and reflective boundary conditions were applied in the z direction. Energy minimization was carried out via the steepest descent algorithm to optimize the geometry of the model, and structural relaxation was performed under a canonical ensemble through the Nose–Hoover thermostat. To investigate the reaction between trimesoyl chloride and piperazine molecules surrounding a single pore, the free energy difference ΔG was calculated in the MD simulations between two specific scenarios before and after the reaction: (i) when the two unreacted molecules were placed on opposite sides of a pore and ii) when they reacted and formed new bonds across the pore. A higher $|\Delta G|$ indicates that such a reaction becomes much faster. To investigate the permeation effects of three different metal ions, a solution system containing 1000 K^+, 1000 Li^+, and 1000 Mg^{2+} ions was placed on top of the graphene layer. The solution system was first equilibrated under an isothermal–isobaric ensemble at a temperature of 300 K and a pressure of 1 atm for 100 ps. The reacted molecules were placed around the hole with a diameter larger than 0.7 nm in the porous graphene, with the reacted site remaining fixed during the equilibrium process. The whole system, including the porous graphene, reacted molecules, and metal ions, was then relaxed under a canonical ensemble at 300 K for 500 ps. In the permeation simulation, while the reacted molecules were freed, a constant velocity was applied on the sheet to allow the metal ions to pass across the porous graphene. The differences in energy required to pass through the pore were calculated before and after permeation. The number and type of metal ions were recorded during this process.

Data availability

The authors declare that the data supporting the findings of this study are available within the paper and its supplementary information files. The source data is provided as a source data file Source data are provided with this paper.

References

1. Zuo, P. et al. Near-frictionless ion transport within triazine framework membranes. *Nature* **617**, 299–305 (2023).
2. Yang, Y. et al. Large-area graphene-nanomesh/carbon-nanotube hybrid membranes for ionic and molecular nanofiltration. *Science* **364**, 1057–1062 (2019).
3. Wang, J. et al. Cascaded compression of size distribution of nanopores in monolayer graphene. *Nature* **623**, 956–963 (2023).
4. Hsu, K.-J. et al. Graphene membranes with pyridinic nitrogen at pore edges for high-performance CO_2 capture. *Nat. Energy* **9**, 964–974 (2024).
5. Nair, R. R., Wu, H. A., Jayaram, P. N., Grigorieva, I. V. & Geim, A. K. Unimpeded permeation of water through helium-leak–tight graphene-based membranes. *Science* **335**, 442–444 (2012).
6. Bae, S. et al. Roll-to-roll production of 30-inch graphene films for transparent electrodes. *Nat. Nanotechnol.* **5**, 574–578 (2010).
7. Kidambi, P. R. et al. A scalable route to nanoporous large-area atomically thin graphene membranes by roll-to-roll chemical vapor deposition and polymer support casting. *ACS Appl. Mater. Interfaces* **10**, 10369–10378 (2018).
8. Mi, B. Scaling up nanoporous graphene membranes. *Science* **364**, 1033–1034 (2019).
9. Karnik, R. N. Breakthrough for protons. *Nature* **516**, 173–174 (2014).
10. Bunch, J. S. et al. Impermeable atomic membranes from graphene sheets. *Nano Lett.* **8**, 2458–2462 (2008).
11. Morelos-Gomez, A. et al. Effective NaCl and dye rejection of hybrid graphene oxide/graphene layered membranes. *Nat. Nanotechnol.* **12**, 1083–1088 (2017).
12. Wang, L. et al. Fundamental transport mechanisms, fabrication and potential applications of nanoporous atomically thin membranes. *Nat. Nanotechnol.* **12**, 509–522 (2017).
13. Park, H. B., Kamcev, J., Robeson, L. M., Elimelech, M. & Freeman, B. D. Maximizing the right stuff: the trade-off between membrane permeability and selectivity. *Science* **356**, eaab0530 (2017).
14. Liu, Q., Liu, Y. & Liu, G. Simulation of cations separation through charged porous graphene membrane. *Chem. Phys. Lett.* **753**, 137606 (2020).
15. Sint, K., Wang, B. & Král, P. Selective ion passage through functionalized graphene nanopores. *J. Am. Chem. Soc.* **130**, 16448–16449 (2008).
16. Surwade, S. P. et al. Water desalination using nanoporous single-layer graphene. *Nat. Nanotechnol.* **10**, 459–464 (2015).
17. Zhang, D. et al. Bioinspired large-area atomically-thin graphene membranes. *Adv. Funct. Mater.* **34** 2307419 (2023).
18. Kidambi, P. R. et al. Nanoporous atomically thin graphene membranes for desalting and dialysis applications. *Adv. Mater.* **29** 1700277 (2017).
19. He, G. et al. Synergistic CO_2-sieving from polymer with intrinsic microporosity masking nanoporous single-layer graphene. *Adv. Funct. Mater.* **30**, 2003979 (2020).
20. Qin, Y. et al. Ultrafast nanofiltration through large-area single-layered graphene membranes. *ACS Appl. Mater. Interfaces* **9**, 9239–9244 (2017).
21. Jang, D., Idrobo, J.-C., Laoui, T. & Karnik, R. Water and solute transport governed by tunable pore size distributions in nanoporous graphene membranes. *ACS Nano* **11**, 10042–10052 (2017).
22. Cheng, P. et al. Facile size-selective defect sealing in large-area atomically thin graphene membranes for sub-nanometer scale separations. *Nano Lett.* **20**, 5951–5959 (2020).
23. Zhao, J. et al. Etching gas-sieving nanopores in single-layer graphene with an angstrom precision for high-performance gas mixture separation. *Sci. Adv.* **5**, eaav1851 (2019).
24. He, G. et al. High-permeance polymer-functionalized single-layer graphene membranes that surpass the postcombustion carbon capture target. *Energy Environ. Sci.* **12**, 3305–3312 (2019).
25. Huang, S. et al. In situ nucleation-decoupled and site-specific incorporation of Å-scale pores in graphene via epoxidation. *Adv. Mater.* **34**, 2206627 (2022).
26. Schlichting, K.-P. & Poulikakos, D. Selective etching of graphene membrane nanopores: from molecular sieving to extreme permeance. *ACS Appl. Mater. Interfaces* **12**, 36468–36477 (2020).
27. Cheng, C., Iyengar, S. A. & Karnik, R. Molecular size-dependent subcontinuum solvent permeation and ultrafast nanofiltration across nanoporous graphene membranes. *Nat. Nanotechnol.* **16**, 989–995 (2021).
28. Cheng, C., Jiang, G., Simon, G. P., Liu, J. Z. & Li, D. Low-voltage electrostatic modulation of ion diffusion through layered graphene-based nanoporous membranes. *Nat. Nanotechnol.* **13**, 685–690 (2018).
29. Cohen-Tanugi, D. & Grossman, J. C. Water permeability of nanoporous graphene at realistic pressures for reverse osmosis desalination. *J. Chem. Phys.* **141**, 074704 (2014).
30. Jiang, D.-e, Cooper, V. R. & Dai, S. Porous graphene as the ultimate membrane for gas separation. *Nano Lett.* **9**, 4019–4024 (2009).
31. Cohen-Tanugi, D. & Grossman, J. C. Water desalination across nanoporous graphene. *Nano Lett.* **12**, 3602–3608 (2012).
32. Suk, M. E. & Aluru, N. R. Water transport through ultrathin graphene. *J. Phys. Chem. Lett.* **1**, 1590–1594 (2010).
33. Shahbabaei, M., Tang, D. & Kim, D. Simulation insight into water transport mechanisms through multilayer graphene-based membrane. *Comp. Mater. Sci.* **128**, 87–97 (2017).
34. Jang, D., Bakli, C., Chakraborty, S. & Karnik, R. Molecular self-assembly enables tuning of nanopores in atomically thin graphene membranes for highly selective transport. *Adv. Mater.* **34**, e2108940 (2022).
35. Shen, L. et al. Highly porous nanofiber-supported monolayer graphene membranes for ultrafast organic solvent nanofiltration. *Sci. Adv.* **7**, eabg6263 (2021).
36. Zhou, Z. et al. Electrochemical-repaired porous graphene membranes for precise ion-ion separation. *Nat. Commun.* **15**, 4006 (2024).

37. Zhang, M. et al. Controllable ion transport by surface-charged graphene oxide membrane. *Nat. Commun.* **10**, 1253 (2019).
38. Guo, B.-B. et al. Double charge flips of polyamide membrane by ionic liquid-decoupled bulk and interfacial diffusion for on-demand nanofiltration. *Nat. Commun.* **15**, 2282 (2024).
39. Villalobos, L. F. et al. Bottom-up synthesis of graphene films hosting atom-thick molecular-sieving apertures. *Proc. Natl Acad. Sci. USA* **118**, e2022201118 (2021).
40. Huang, S. et al. Single-layer graphene membranes by crack-free transfer for gas mixture separation. *Nat. Commun.* **9**, 2632 (2018).
41. Goethem, C. V. et al. Advancing molecular sieving via Å-scale pore tuning in bottom-up graphene synthesis. *ACS Nano* **18**, 5730–5740 (2024).
42. Huang, S. et al. Millisecond lattice gasification for high-density CO_2- and O_2-sieving nanopores in single-layer graphene. *Sci. Adv.* **7**, eabf0116 (2021).
43. Meng, Q.-W. et al. Enhancing ion selectivity by tuning solvation abilities of covalent-organic-framework membranes. *Proc. Natl Acad. Sci. USA* **121**, e2316716121 (2024).
44. Esfandiar, A. et al. Size effect in ion transport through angstrom-scale slits. *Science* **358**, 511–513 (2017).
45. Yuan, S. et al. Facile synthesis of Kevlar nanofibrous membranes via regeneration of hydrogen bonds for organic solvent nanofiltration. *J. Membr. Sci.* **573**, 612–620 (2019).
46. Bai, Y. et al. Microstructure optimization of bioderived polyester nanofilms for antibiotic desalination via nanofiltration. *Sci. Adv.* **9**, eadg6134 (2023).
47. Shen, L. et al. Polyamide-based membranes with structural homogeneity for ultrafast molecular sieving. *Nat. Commun.* **13**, 500 (2022).
48. Peng, Q. et al. Extreme Li-Mg selectivity via precise ion size differentiation of polyamide membrane. *Nat. Commun.* **15**, 2505 (2024).
49. Zhou, Z. et al. Ultrathin polyamide membranes enabled by spin-coating assisted interfacial polymerization for high-flux nanofiltration. *Sep. Purif. Technol.* **288**, 120648 (2022).
50. Wang, Z. et al. Ultrathin polyamide nanofiltration membranes with tunable chargeability for multivalent cation removal. *J. Membr. Sci.* **642**, 119971 (2022).
51. Freger, V. Nanoscale heterogeneity of polyamide membranes formed by interfacial polymerization. *Langmuir* **19**, 4791–4797 (2003).
52. Guo, J. et al. Ultra-permeable dual-mechanism-driven graphene oxide framework membranes for precision ion separations. *Angew. Chem. Inter. Ed.* **62**, e202302931 (2023).
53. Dakhchoune, M. et al. Rapid gas transport from block-copolymer templated nanoporous carbon films. *Ind. Eng. Chem. Res.* **60**, 16100–16108 (2021).
54. Kumar, R. et al. Downstream recovery of Li and value-added metals (Ni, Co, and Mn) from leach liquor of spent lithium-ion batteries using a membrane-integrated hybrid system. *Chem. Eng. J.* **447**, 137507 (2022).
55. Lu, J. et al. Efficient metal ion sieving in rectifying subnanochannels enabled by metal–organic frameworks. *Nat. Mater.* **19**, 767–774 (2020).

Acknowledgements

This study was financed by the National Key Research and Development Program of China (2023YFC3207404, 2022YFA1205603) and the National Natural Science Foundation of China (Nos. 52370137 and 52100086). Additionally, we would like to thank the Analytical and Testing Center of Huazhong University of Science and Technology (HUST) for providing the experimental measurements and the School of Environmental Science and Engineering of HUST for supplying the instruments for material analysis. P.J. acknowledges the Research Foundation Flanders (FWO) research project (1262323N) and the FWO Tournesol project (VS00724N).

Author contributions

P.J. and S.Y. supervised the project. P.J. and Z.D. designed, fabricated, and tested the graphene membranes. K.V.A. developed the graphene synthesis procedure. H.W., K.V.A. and J.Y. participated in the discussion. S.Y., P.J. and Z.D. wrote the paper. H.W. and K.V.A. read and revised the paper.

Competing interests

The authors declare no competing interests.

Additional information

Supplementary information The online version contains supplementary material available at https://doi.org/10.1038/s41467-025-59625-1.

Correspondence and requests for materials should be addressed to Pengrui Jin, Shushan Yuan or Huanting Wang.

Peer review information *Nature Communications* thanks Chi Cheng, Rohit Karnik and the other, anonymous, reviewer(s) for their contribution to the peer review of this work. A peer review file is available.